nature photonics

ARTICLES

PUBLISHED ONLINE: 9 MARCH 2015 | DOI: 10.1038/NPHOTON.2015.24

Imaging deep within a scattering medium using collective accumulation of single-scattered waves

Sungsam Kang[1†], Seungwon Jeong[1†], Wonjun Choi[1], Hakseok Ko[1], Taeseok D. Yang[1], Jang Ho Joo[2], Jae-Seung Lee[2], Yong-Sik Lim[3], Q-Han Park[1] and Wonshik Choi[1,4*]

Optical microscopy suffers from a loss of resolving power when imaging targets are embedded in thick scattering media because of the dominance of strong multiple-scattered waves over waves scattered only a single time by the targets. Here, we present an approach that maintains full optical resolution when imaging deep within scattering media. We use both time-gated detection and spatial input–output correlation to identify those reflected waves that conserve in-plane momentum, which is a property of single-scattered waves. By implementing a superradiance-like collective accumulation of the single-scattered waves, we enhance the ratio of the single scattering signal to the multiple scattering background by more than three orders of magnitude. An imaging depth of 11.5 times the scattering mean free path is achieved with a near-diffraction-limited resolution of 1.5 μm. Our method of distinguishing single- from multiple-scattered waves will open new routes to deep-tissue imaging and studying the physics of the interaction of light with complex media.

In the life sciences and biomedicine, optical imaging is extensively used to examine specimens, as it allows for the non-invasive investigation of living specimens and provides a spatial resolution high enough for intracellular organelles to be identified[1]. Within the electromagnetic spectrum, visible light occupies the highest energy band (that is, the shortest wavelength) that does not damage biological molecules. As a result, optical imaging offers better resolving power than other non-invasive techniques such as microwave and ultrasound imaging[2]. However, its imaging depth has remained extremely shallow because of multiple elastic light scattering, which irregularly changes the propagation direction of light waves carrying information about the object. The scattering mean free path (MFP) l_s, defined as the average distance between successive scattering events, is only ~100 μm in typical biological tissues and this sets the depth limit for conventional bright-field imaging[1].

In the context of coherent imaging, three main approaches have been followed to address the detrimental effects of multiple light scattering. In the first, ballistic photons are selectively detected in a transillumination[3–5] or reflection geometry[6] using temporal and/or coherence gating. Although the spatial resolution of this approach can be high, its working depth tends to be shallow due to the exponential attenuation of signal intensity. As a consequence, the imaging depth at which the diffraction-limited spatial resolution is guaranteed has so far only been a few MFPs. The second approach uses those waves that are scattered multiple times at small deflection angles so that the overall propagation direction is maintained[7–12]. The imaging depth of this intermediate approach is better than the first approach, but degradation of the spatial resolution is inevitable. For example, deep-tissue imaging methods such as photoacoustic microscopy can identify target objects located much deeper than ten MFPs with limited spatial resolution[10], and studies have been carried out to enhance this spatial resolution so it is comparable to optical resolution[11,12]. The third approach exploits multiple-scattered waves in full. For instance, multiple-scattered waves have been used on the basis of photon diffusion theory[13,14]. With this, an imaging depth of a few centimetres has

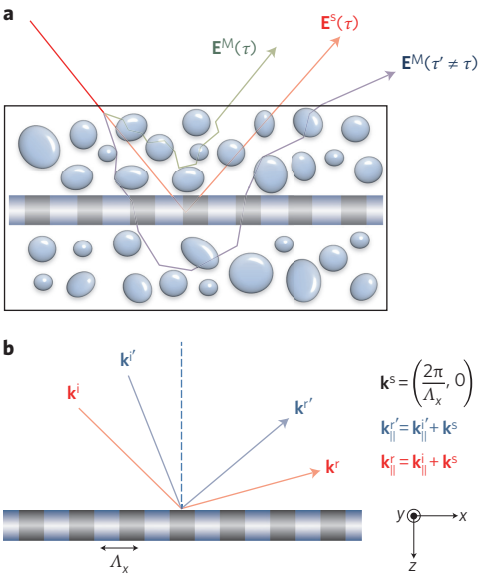

Figure 1 | Schematic diagram for the collective enhancement of single-scattered waves. a, Classification of reflected waves. $\mathbf{E}^{S}(\tau)$: electric field of a wave scattered once by a target object located at a depth of $c\tau/2$, where τ and c are the time of flight from the surface and the speed of light in the medium, respectively. $\mathbf{E}^{M}(\tau)$: multiple-scattered waves with the same time of flight as the single-scattered waves. $\mathbf{E}^{M}(\tau' \neq \tau)$: multiple-scattered waves with a time of flight that is different from τ. **b**, In-plane momentum conservation property of single-scattered waves. $\mathbf{k}^{i}$ and $\mathbf{k}^{r}$ are wavevectors of incident and reflected waves, respectively, for one illumination angle, and $\mathbf{k}^{i'}$ and $\mathbf{k}^{r'}$ are those for another illumination angle. $\mathbf{k}_{\parallel}^{i}$, $\mathbf{k}_{\parallel}^{r}$, $\mathbf{k}_{\parallel}^{i'}$ and $\mathbf{k}_{\parallel}^{r'}$ are the components of the associated wavevectors parallel to the x–y plane. The reflected waves gain a lateral momentum of $\mathbf{k}^{s} = \left((2\pi/\Lambda_x), 0\right)$ of the target object, where Λ_x is the period of the structure along the x-axis, irrespective of incident momentum.

[1]Department of Physics, Korea University, Seoul 136-701, Korea. [2]Department of Materials Science and Engineering, Korea University, Seoul 136-701, Korea. [3]Department of Nano Science and Mechanical Engineering and Nanotechnology Research Center, Konkuk University, Chungbuk 380-701, Korea. [4]Center for Molecular Spectroscopy and Dynamics, Seoul 136-701, Korea. †These authors contributed equally to this work. *e-mail: wonshik@korea.ac.kr

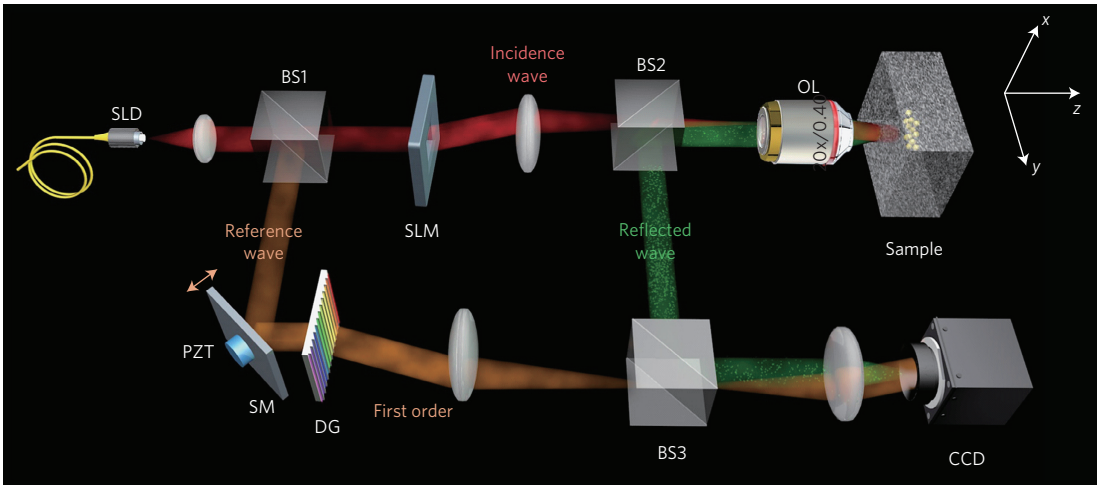

Figure 2 | Experimental schematic diagram of the CASS microscope. SLD, diode laser; OL, objective lens; BS1, BS2 and BS3, beamsplitters; SLM, spatial light modulator (working in reflection mode, but indicated here as a transmission mode for simplicity); DG, diffraction grating (an aperture was used to select the first-order diffracted wave); SM, path length scanning mirror; CCD, charge-coupled device camera. For clarity, red, green and dark gold are used to indicate incident, reflected and reference waves, respectively, although their wavelengths are the same.

been possible, but with a limited spatial resolution of a few millimetres. Alternatively, the wave correlation of speckled waves generated by multiple light scattering[15–20] can be used. This works for an arbitrary thickness of scattering layer. However, it is not yet possible for these types of wave correlation approach to image targets embedded within a scattering medium. In the context of inelastic scattering, other types of deep-tissue imaging method have been pursued in recent decades. For example, two-photon and three-photon microscopy techniques have been used successfully to image targets located at a depth of a few MFPs, benefiting from the long excitation wavelength reducing the effect of multiple light scattering[21,22].

Principle

To obtain a high-resolution image for a target object embedded within a scattering medium, it is necessary to extract single-scattered waves. These are waves that have been scattered only once by the target object, so they retain object information. However, when the target object is located deep inside the scattering layers, this is an extremely difficult task. For an object located at a depth of $11l_s$, for example, the single-scattered wave intensity is attenuated by a factor of $e^{-22} \cong 10^{-10}$. As a consequence, most of the light waves are reflected back without interacting with the target object, and those that do interact with the object tend to lose object information on their way out. In this Article we present a method to enhance single-scattered waves embedded within a background of random multiple-scattered waves. Using what we term 'collective accumulation of single scattering' (CASS) microscopy, we identify targets embedded at a depth of $\sim 11.5l_s$ with almost no loss of spatial resolution. With this method we combine a time-gated detection and a spatial input–output wave correlation. The time-gated detection serves to screen out a large fraction of multiple-scattered waves, which have a time of flight that is different from that of the single-scattered waves (Fig. 1a). According to our measurements, the time-gated detection attenuates the intensity of multiple-scattered waves by a few orders of magnitude (see Supplementary Section IV). However, multiple-scattered waves with the same time of flight as the single-scattered waves were still dominant for targets located deeper than a few MFPs.

To further enhance the detection of single-scattered waves we used spatial input–output correlation. Specifically, we exploited the fact that the input–output response for single scattering preserves in-plane momentum, while the response for multiple scattering does not. To clarify, let us consider a thin periodic structure with wavevector $\mathbf{k}^s$ in reciprocal space (Fig. 1b). For a single-scattered wave, the in-plane wavevector of the reflected wave $\mathbf{k}_{\|}^r = (k_x^r,\ k_y^r)$ (which is the component of the wavevector of reflected wave parallel to the x–y plane) is the addition of $\mathbf{k}^s$ to the in-plane wavevector of the incident wave $\mathbf{k}_{\|}^i$, regardless of the direction of the incident wave vector. In our study, we measured the map of reflected waves for $N_{tot} = 2{,}500$ different incident wavevectors. By coherently adding the relative complex amplitudes for pairs of input–output waves with the same momentum difference, $\mathbf{k}^s = \mathbf{k}_{\|}^r - \mathbf{k}_{\|}^i$, we could collectively accumulate the single-scattered waves associated with the $\mathbf{k}^s$ component of the object function. This leads to enhancement of the single scattering intensity on the order of N_{tot}^2. In fact, this signal increase behaviour is similar to that of superradiance, in which the radiations of dipoles are coherently added[23]. Considering that the intensity of multiple-scattered waves scales with N_{tot} due to incoherent addition, we could enhance the relative intensity of single- to multiple-scattered waves by a factor of N_{tot}. With the combination of temporal gating and spatial input–output correlation, CASS microscopy could extract single-scattered waves attenuated by a factor of up to 10^{10} by scattering media. On a separate note, in acoustic imaging those waves that have quadratic phase retardation for source–detector separation were considered to be single-scattered waves, which is the case under the Fresnel approximation[24]. This approach is similar to CASS microscopy in that input–output correlation is used to identify single-scattered waves, but it works only for paraxial waves.

Experimental set-up and image processing

We constructed a reflection-mode interferometric microscope (Fig. 2 and Supplementary Section IV) in which a superluminescent diode laser (centre wavelength of 800 nm; bandwidth of 25 nm) was used as a low-coherence light source to provide temporal gating. A spatial light modulator (SLM) was installed to control the angle of illumination to the sample. $N_{tot} = 2{,}500$ phase ramps were written on the SLM so that the incident wavevectors covered all the orthogonal input modes for the field of view of $70 \times 70\ \mu m^2$. The incident wave was delivered to the sample plane via an objective lens (×20, NA = 0.4). The same lens captured the reflected wave from the sample and subsequently delivered it to the camera. The laser power at the sample plane was ~0.1 mW. The laser output reflected off beamsplitter BS1 served as a reference wave and interfered with

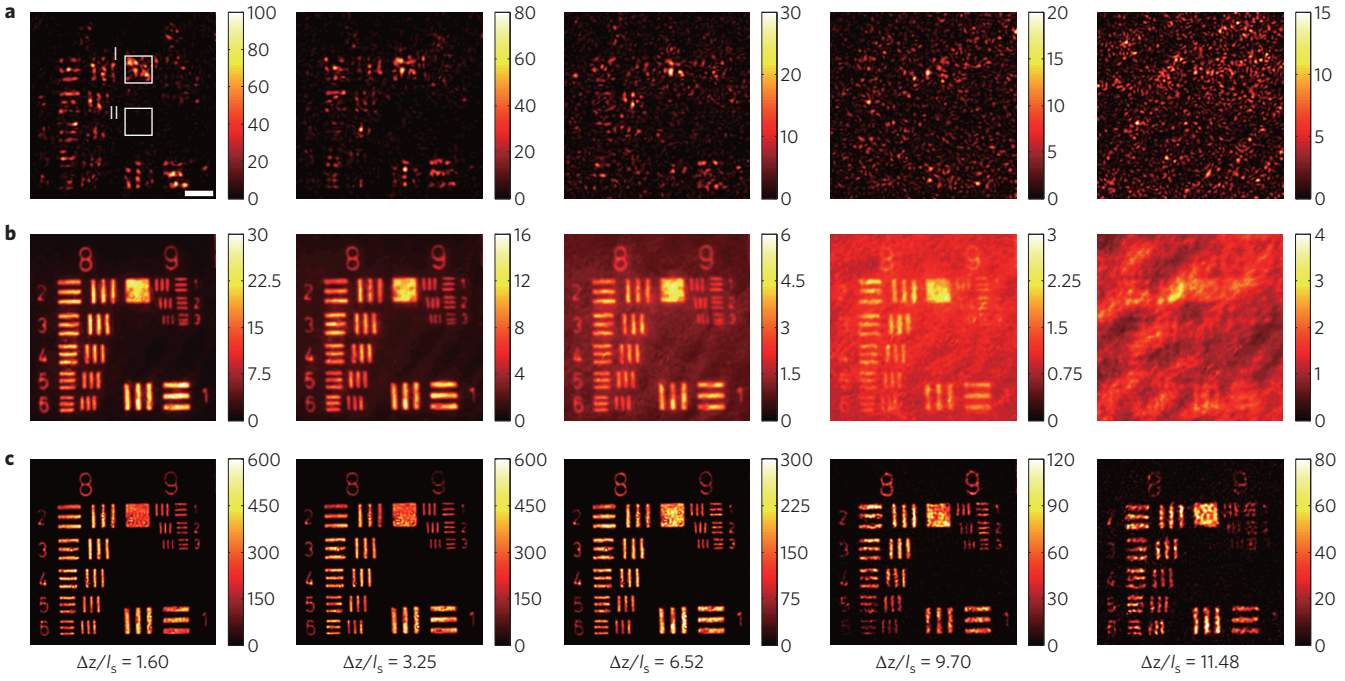

Figure 3 | Demonstration of near diffraction-limited imaging in a thick scattering medium. a, Single-shot images under normal illumination. From the left, the thicknesses of the scattering layers are $1.60l_s$, $3.25l_s$, $6.52l_s$, $9.70l_s$ and $11.48l_s$, respectively. **b**, Angular compounding images for the same thicknesses. **c**, Reconstructed images using CASS for the same thicknesses. All images are normalized by the mean values in the region indicated by square box II, where there was no chrome coating. Because multiple-scattered waves were mostly present in this region, the colour bars correspond to the ratio between the intensities of single- and multiple-scattered waves. Scale bar, 10 μm. The colour bars indicate the ratio between the signal intensity and that in the background region.

the reflected wave at the camera. By controlling the optical path length of the reference wave using a scanning mirror, we selectively recorded reflected waves with the same time of flight as that of the reference wave with a temporal resolution of 76 fs, the coherence time of the light source. In the absence of multiple scattering, this temporal gating corresponds to a depth resolution of ~11.4 μm. Both the incident and reference waves were linearly polarized, and reflected waves with the same polarization as the reference wave were selectively recorded because interference occurs between the same polarization components of reflected and reference waves. The focal plane of the objective lens and the target depth set by the temporal gating were matched. A diffraction grating was used to set the propagation direction of the reference wave oblique relative to the optical axis, and a complex field map for the reflected wave was obtained using a Hilbert transform[25]. As a test sample, we fabricated a slab of scattering media by dispersing polystyrene beads (diameter of 1 μm) in polydimethylsiloxane (PDMS), and pasted this layer onto the United States Air Force (USAF) resolution target. Typical samples used in the experiment had $l_s = 102$ μm and a transport MFP of 1.18 mm, values that approximate those for typical biological tissues.

For each incident wavevector of unit amplitude, the time-gated complex field map of the reflected wave $u(x, y; \mathbf{k}_{\|}^{i}, \tau)$ was recorded at the sample plane (x–y plane) for arrival time τ (set by the optical path length of the reference wave). Using the N_{tot} recorded images taken at a given arrival time, the wide-field time-gated reflection matrix $\mathcal{U}(\mathbf{k}_{\|}^{r}; \mathbf{k}_{\|}^{i}, \tau)$ was constructed by taking the Fourier transform of $u(x, y; \mathbf{k}_{\|}^{i}, \tau)$ (see Methods for matrix construction). Representative images of the reflected waves for various phase ramps and the constructed reflection matrix are shown in Fig. 6.

Because the reflected waves include both single- and multiple-scattered waves, $\mathcal{U}$ can be decomposed into $\mathcal{U} = \mathcal{U}_S + \mathcal{U}_M$, where $\mathcal{U}_S$ is the single-scattering matrix carrying the object information and $\mathcal{U}_M$ is the multiple-scattering matrix. To extract $\mathcal{U}_S$ from $\mathcal{U}$, we made use of the property of single scattering described in Fig. 1b. For single scattering, time-gated detection captures signals from a thin layer with a thickness corresponding to the temporal gating. The target object can then be described by the two-dimensional object function $f(x,y)$ and its associated object transfer function $\mathcal{F}(\mathbf{k}^s)$, which is the two-dimensional Fourier transform of $f(x,y)$. Wavevector $\mathbf{k}^s = (k_x^s, k_y^s)$ describes the spatial frequency of the target object at the sample plane. As explained in Fig. 1b, U_S is related to $\mathcal{F}(\mathbf{k}^s)$ by

$$\mathcal{U}_S(\mathbf{k}_{\|}^{r}; \mathbf{k}_{\|}^{i}) \approx \mathcal{F}(\mathbf{k}_{\|}^{r} - \mathbf{k}_{\|}^{i}) = \mathcal{F}(\mathbf{k}^s) \quad (1)$$

This indicates that the matrix elements of U_S with the same $\mathbf{k}^s = \mathbf{k}_{\|}^{r} - \mathbf{k}_{\|}^{i}$ originate from the same spatial frequency component of $\mathcal{F}$. Note that those $\mathcal{F}(\mathbf{k}^s)$ with the same $\mathbf{k}^s$ are not equal in their amplitudes because the reflectance of the target object varies depending on the incident angle. However, their phases are equal, so coherent addition is possible.

Although $\mathcal{U}_S$ follows the specific rule described in equation (1), the elements in $\mathcal{U}_M$ are statistically random because there is almost no correlation between multiple-scattered waves of different incident angles. To make use of this distinction, we added those matrix elements with the same momentum difference:

$$\sum_{\mathbf{k}_{\|}^{i}} \mathcal{U}(\mathbf{k}_{\|}^{r}; \mathbf{k}_{\|}^{i}) \approx N(\mathbf{k}^s)\mathcal{F}(\mathbf{k}^s) + \sum_{\mathbf{k}_{\|}^{i}} \mathcal{U}_M \quad (2)$$

Here, $\sum_{\mathbf{k}_{\|}^{i}}$ indicates the summation of matrix elements with the same $\mathbf{k}^s$, and $N(\mathbf{k}^s)$ is the number of elements involved in the summation. $N(\mathbf{k}^s)$ is equal to N_{tot} at $\mathbf{k}^s = 0$ and becomes smaller as $|\mathbf{k}^s|$ increases (see Supplementary Section II for the map of $N(\mathbf{k}^s)$). As this relationship indicates, single-scattering elements are added in phase and multiple-scattering elements are accumulated incoherently. As a result, the signal intensity of single-scattered waves

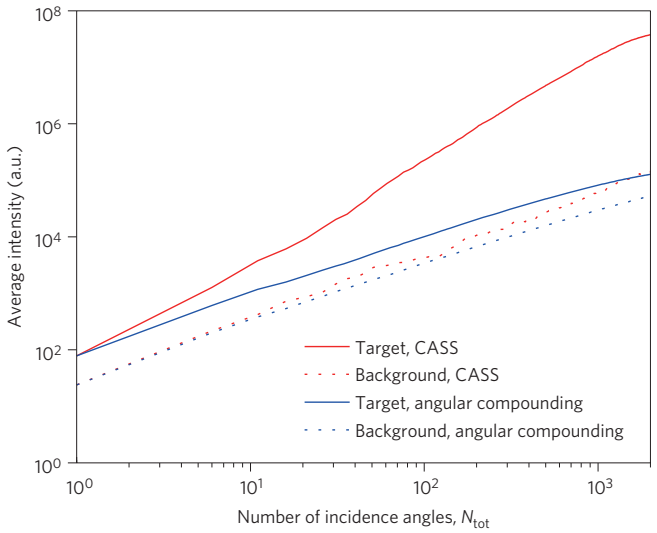

Figure 4 | Performance of single-scattering enhancement depending on the number of incidence angles, N_{tot}. Average intensities are plotted for the target (square box I in Fig. 3a) and background (square box II in Fig. 3a) before normalization. Solid and dashed red curves: average intensities in the target and background, respectively, for CASS. Solid and dashed blue curves: average intensities in the target and background, respectively, for the angular compounding method. The thickness of the scattering layer used in this plot is $9.7l_s$. The slopes of the solid red and blue lines were measured to be 1.82 and 0.92, respectively.

is proportional to $N(\mathbf{k}^s)^2$ while that of the multiple-scattered waves increase with $N(\mathbf{k}^s)$. Even though the individual matrix elements of $\mathcal{U}_M$ are much larger than those of $\mathcal{U}_S$, the operation in equation (2) enables the contribution of single scattering to dominate that of multiple scattering as long as there are sufficient matrix elements available to be added. Once $\mathcal{F}(\mathbf{k}^s)$ is identified, we can reconstruct an object image by taking its inverse Fourier transform. Moreover, we could extract $\mathcal{U}_S$ (embedded in $\mathcal{U}$) by multiplication of the incident waves and the object function (Fig. 6d) and also obtain $\mathcal{U}_M$ by subtracting the reconstructed $\mathcal{U}_S$ from $\mathcal{U}$. In the image reconstruction process with experimental data, there are uncontrolled phase shifts induced by the instability of the interferometer and the sample-induced aberration, both of which cause angle-dependent phase retardations. We added an overall phase shift to each individual angle-dependent complex field map in such a way as to maximize the total intensity of the reconstructed images. This additional process led to optimal signal growth and effectively dealt with the sample-induced aberration.

Imaging a target behind a thick scattering layer

Figure 3 shows reconstructed object images for various thicknesses of scattering layer placed on top of the USAF target. As a point of reference, we present individual time-gated images and angular compounding images, which are the summation of the intensity maps from the N_{tot} complex field maps. This angular compounding is a conventional method to suppress the effect of multiple scattering[26]. However, previous methods were implemented in the point-scanning mode of optical coherence tomography, whereas our angular compounding works as a wide-field imaging mode. Individual time-gated images were unable to visualize fine details in the ninth group of the USAF target (for which the smallest line pair separation is 1.56 μm), even at a depth of $1.60l_s$. With an increase in thickness, the presented angular compounding method could cope with the effect of multiple scattering to a certain extent and revealed the fine details up to a depth of $\sim 7l_s$. Indeed, these are the first wide-field angular compounding images presented to date. Beyond this depth, however, the angular compounding method was unable to produce images of sufficient resolution. However, CASS microscopy produced a sharp resolution for the ninth group of the USAF target in layers up to $11.5l_s$ thick, a thickness comparable to the length of the transport MFP. To our knowledge, this is the deepest target ever imaged at diffraction-limited optical resolution.

The difference between CASS and the angular compounding method is evident when we compare the ratio between the signal intensity at the resolution target (square box I in Fig. 3a) and that in the background region (square box II in Fig. 3a), where there were mainly multiple-scattered waves (the colour bar in Fig. 3 indicates this ratio). With an increase in thickness, this ratio quickly decreases in the angular compounding images as the intensity of multiple-scattered waves starts to dominate over the single-scattering intensity. However, with CASS the signal-to-background ratio remains at 100 or more, even in the $10l_s$-thick samples, as a consequence of the collective addition of single-scattered waves.

To quantify the performance of CASS in collective single-scattering enhancement, we plotted the intensity of the reconstructed image at square box I (in which $\mathbf{k}^s$ is small so $N(\mathbf{k}^s) \approx N_{tot}$) as a function of the number of incident angles (see Supplementary Section III for representative images at various N_{tot}). The absolute square of the left-hand side of equation (2) was plotted for CASS to show the growth of signal with N_{tot}, and no normalization factor was applied to the angular compounding method. We observed that the single-scattering intensity grew in proportion to $N_{tot}^{1.82}$ (solid red curve in Fig. 4), very close to the theoretical expectation of N_{tot}^2. The same plot for the angular compounding method produced a signal growth rate of $N_{tot}^{0.92}$ (solid blue line in Fig. 4).

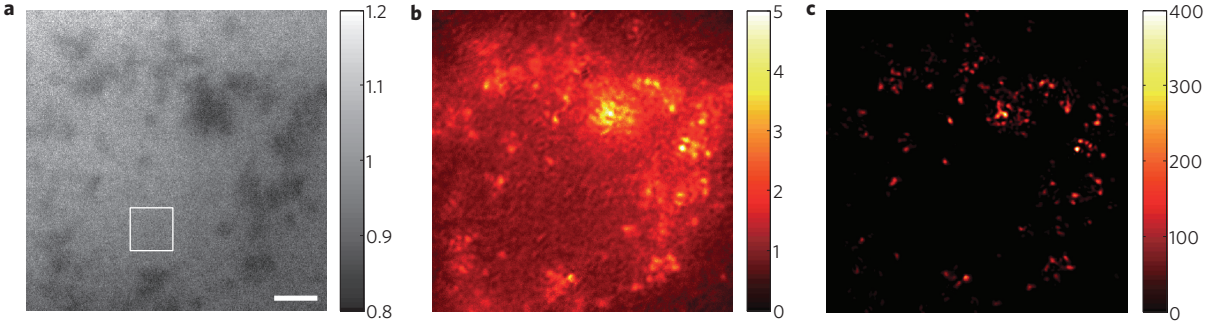

Figure 5 | CASS imaging of 2-μm-diameter beads embedded in thick rat brain tissue. a, Transmission image taken with the light source (light-emitting diode, $\lambda = 780$ nm) illuminating the specimen from below. The target sample comprised 2-μm-diameter gold-coated beads sandwiched between two 560-μm-thick rat brain slices. **b**, Angular compounding image for the sample in **a**. **c**, CASS image for the sample in **a**. Scale bar, 10 μm. The colour bars show the signal intensity and are normalized by the background region containing no beads, as indicated by the white box in **a**.

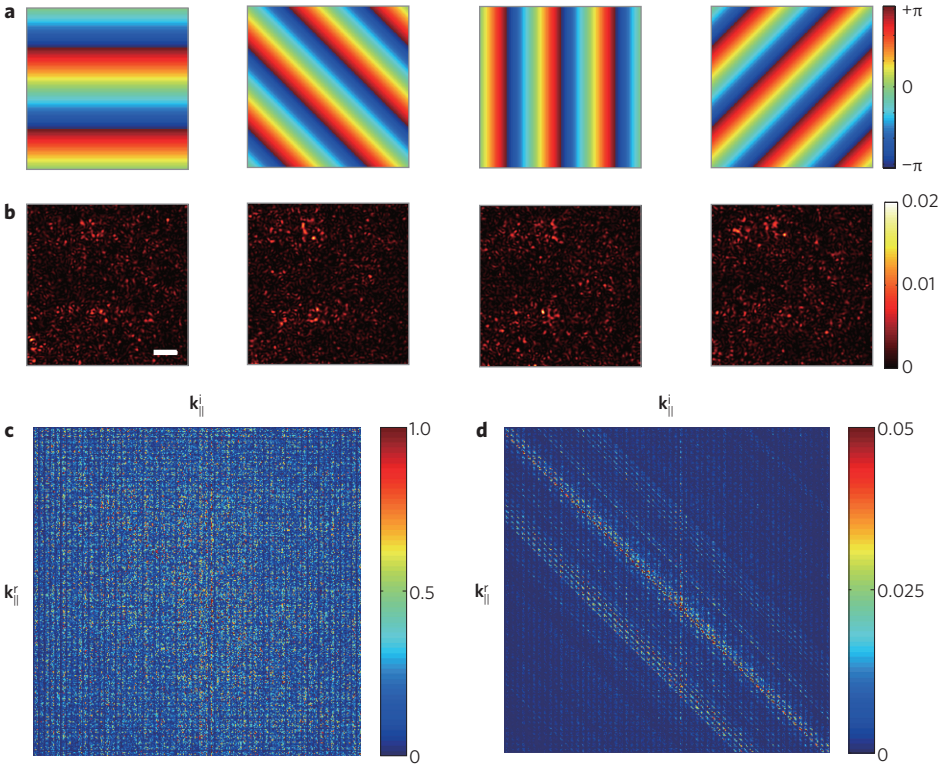

Figure 6 | Measurement and construction of the time-gated reflection matrix. a,**b**, Representative phase ramps written on the SLM and the time-gated amplitude maps of the reflected waves, respectively. Phase maps were acquired simultaneously, but are not shown here. The colour bars measure phase in radians and amplitude in arbitrary units. Scale bar, 10 μm. **c**, Time-gated reflection matrix $\mathcal{U}$, constructed from 2,500 complex field maps. Column and row indices are $\mathbf{k}_{\parallel}^{i}$ and $\mathbf{k}_{\parallel}^{r}$, respectively. **d**, Single-scattering matrix $\mathcal{U}_S$ extracted from $\mathcal{U}$ using equation (2). Colour bars in **c** and **d** measure amplitude in arbitrary units.

Considering that the signal-to-noise ratio (SNR) is determined by the ratio between the single-scattering intensity and multiple-scattering fluctuations, the SNR for angular compounding method scales with $\sqrt{N_{tot}}$. As spatial intensity fluctuations due to multiple scattering grow with N_{tot} in CASS due to the addition of random complex fields[27], the theoretical SNR of our method scales with N_{tot}. For high spatial frequencies, the SNR is determined by $N(\mathbf{k}^{s})$, instead of N_{tot}.

Imaging targets embedded within biological tissues

We next demonstrated the superior performance of CASS microscopy compared to angular compounding for the imaging of small particles embedded in inhomogeneous biological tissues (Fig. 5). We prepared gold-coated silica beads (diameter, 2 μm) and sandwiched them between two slices of 560-μm-thick rat brain tissue extracted from a three-day-old Sprague Dawley rat. The bright-field image (Fig. 5a) obtained with illumination by light-emitting diodes from the bottom of the sample and the angular compounding image (Fig. 5b) cannot identify the individual beads. However, the CASS image in Fig. 5c clearly shows the individual beads, thus confirming the superior resolving power of CASS over conventional methods (see Supplementary Section IX for control experiments with tissue phantoms, in which the CASS images taken with and without the scattering layer show good agreement). We also demonstrated CASS imaging of the USAF target under 0.9-mm-thick rat brain tissue (Supplementary Fig. S6).

Discussion

We have presented a method to collectively enhance single-scattered waves from a target object embedded in thick scattering media and have experimentally demonstrated near diffraction-limited optical microscopic imaging up to a depth of 11.5 times the scattering MFP. This imaging depth was mostly limited by the detector dynamic range in the present experiment, and could be improved by using a detector with a higher dynamic range than the camera used in the experiment (see Supplementary Section VI for details). For *in vivo* applications, an increase in data acquisition speed would be the next step in order to deal with the decorrelation of scattered waves caused by the dynamics of a scattering medium. The acquisition of 2,500 angle-dependent wide-field images takes ~250 s, mainly due to the slow refresh rate of the wavefront-shaping device used in the present experiment. This technical issue could be resolved by the use of a high-speed wavefront-shaping device as well as a fast camera. Scanning the target depth set by the temporal and focus gating, which is necessary for volumetric imaging, will bring the benefit of high-speed data acquisition. Because our method works for coherent light scattering process, it itself is not applicable to fluorescence imaging, but may be combined with two-photon or three-photon imaging techniques to exploit various contrast mechanisms for specimens. Our method of high-resolution imaging at an unprecedented target depth will lead to advances in the life sciences and biomedicine, in which the shallow imaging depth of conventional optical microscopy is a major obstacle. In addition, the ability to distinguish single- and multiple-scattered waves will open new approaches to studying the physics of the interaction of light with complex media[28].

Methods

Experimental set-up. The following components were used in the experimental set-up (Fig. 2): a super-luminescent diode laser (SLD-331-HP, Superlum), a spatial

light modulator (LCOS-X10468-01, Hamamatsu), an objective lens (Olympus, ×20, NA= 0.4), a charge-coupled device (CCD) camera (LM135M, Lumenera), a diffraction grating (72 lines/mm, Ronchi). Path length scanning of the mirror (SM in Fig. 2) was performed using a piezoelectric transducer (Physik Instrument) attached to the backside of the mirror.

Construction of the time-gated reflection matrix. A series of phase ramps were written on the SLM (Fig. 6a). The incident wave reflected from the SLM gained lateral momentum in such a way as to uniformly cover the k-space within a circle with a radius determined by the numerical aperture (NA) of the system. The complex field map $u(x,y;i,\tau)$ of the reflected wave from the sample was measured for each ith phase ramp (Fig. 6b) and the spectrum $\mathcal{U}(\mathbf{k}_\parallel^r; i)$ of each complex field map calculated using the discrete two-dimensional Fourier transform

$$\mathcal{U}(\mathbf{k}_\parallel^r; i) = \iint u(x, y; i, \tau) e^{-i(k_x^r x + k_y^r y)} \mathrm{d}x\mathrm{d}y \quad (3)$$

In practice, the incident waves prepared by the SLM were not pure plane waves, as the realization of phase ramps in the SLM is imperfect. To address this issue, we separately recorded the incident waves $u_i(x,y;i,\tau)$ and obtained an incidence angle matrix $\mathcal{I}(\mathbf{k}_\parallel^i; i)$ for each phase ramp. From the product of $\mathcal{U} \cdot \mathcal{I}^{-1}$, where $^{-1}$ indicates matrix inversion, we were able to obtain the reflection matrix $\mathcal{U}(\mathbf{k}_\parallel^r; \mathbf{k}_\parallel^i)$, as shown in Fig. 6c. Note that the recording of the incidence angle matrix is a one-time calibration measurement for the given set of phase ramps.

Received 17 October 2014; accepted 28 January 2015; published online 9 March 2015

References

1. Murphy, D. B. *Fundamentals of Light Microscopy and Electronic Imaging* (Wiley-Liss, 2001).
2. Duck, F. A. *Physical Properties of Tissues: A Comprehensive Reference Book* (Elsevier Science, 1990).
3. Hee, M. R. *et al.* Femtosecond transillumination optical coherence tomography. *Opt. Lett.* **18,** 950–952 (1993).
4. Niedre, M. J. *et al.* Early photon tomography allows fluorescence detection of lung carcinomas and disease progression in mice *in vivo*. *Proc. Natl Acad. Sci. USA* **105,** 19126–19131 (2008).
5. Anderson, G. E., Liu, F. & Alfano, R. R. Microscope imaging through highly scattering media. *Opt. Lett.* **19,** 981–983 (1994).
6. Huang, D. *et al.* Optical coherence tomography. *Science* **254,** 1178–1181 (1991).
7. Wu, J., Perelman, L., Dasari, R. R. & Feld, M. S. Fluorescence tomographic imaging in turbid media using early-arriving photons and Laplace transforms. *Proc. Natl Acad. Sci. USA* **94,** 8783–8788 (1997).
8. Wang, L. V. Prospects of photoacoustic tomography. *Med. Phys.* **35,** 5758–5767 (2008).
9. Xu, X., Liu, H. & Wang, L. V. Time-reversed ultrasonically encoded optical focusing into scattering media. *Nature Photon.* **5,** 154–157 (2011).
10. Wang, L. V. & Hu, S. Photoacoustic tomography: *in vivo* imaging from organelles to organs. *Science* **335,** 1458–1462 (2012).
11. Judkewitz, B. *et al.* Speckle-scale focusing in the diffusive regime with time reversal of variance-encoded light (TROVE). *Nature Photon.* **7,** 300–305 (2013).
12. Suzuki, Y., Tay, J. W., Yang, Q. & Wang, L. V. Continuous scanning of a time-reversed ultrasonically encoded optical focus by reflection-mode digital phase conjugation. *Opt. Lett.* **39,** 3441–3444 (2014).
13. Durduran, T. *et al.* Diffuse optical measurement of blood flow, blood oxygenation, and metabolism in a human brain during sensorimotor cortex activation. *Opt. Lett.* **29,** 1766–1768 (2004).
14. Ntziachristos, V., Yodh, A. G., Schnall, M. & Chance, B. Concurrent MRI and diffuse optical tomography of breast after indocyanine green enhancement. *Proc. Natl Acad. Sci. USA* **97,** 2767–2772 (2000).
15. Yaqoob, Z., Psaltis, D., Feld, M. S. & Yang, C. Optical phase conjugation for turbidity suppression in biological samples. *Nature Photon.* **2,** 110–115 (2008).
16. Popoff, S. *et al.* Image transmission through an opaque material. *Nature Commun.* **1,** 81 (2010).
17. Choi, Y. *et al.* Overcoming the diffraction limit using multiple light scattering in a highly disordered medium. *Phys. Rev. Lett.* **107,** 023902 (2011).
18. Bertolotti, J. *et al.* Non-invasive imaging through opaque scattering layers. *Nature* **491,** 232–234 (2012).
19. Katz, O., Small, E. & Silberberg, Y. Looking around corners and through thin turbid layers in real time with scattered incoherent light. *Nature Photon.* **6,** 549–553 (2012).
20. Katz, O., Heidmann, P., Fink, M. & Gigan, S. Non-invasive single-shot imaging through scattering layers and around corners via speckle correlations. *Nature Photon.* **8,** 784–790 (2014).
21. Theer, P., Hasan, M. T. & Denk, W. Two-photon imaging to a depth of 1000 μm in living brains by use of a Ti:Al_2O_3 regenerative amplifier. *Opt. Lett.* **28,** 1022–1024 (2003).
22. Horton, N. G. *et al. In vivo* three-photon microscopy of subcortical structures within an intact mouse brain. *Nature Photon.* **7,** 205–209 (2013).
23. Dicke, R. Coherence in spontaneous radiation processes. *Phys. Rev.* **93,** 99 (1954).
24. Aubry, A. & Derode, A. Random matrix theory applied to acoustic backscattering and imaging in complex media. *Phys. Rev. Lett.* **102,** 084301 (2009).
25. Choi, Y., Yang, T. D., Lee, K. J. & Choi, W. Full-field and single-shot quantitative phase microscopy using dynamic speckle illumination. *Opt. Lett.* **36,** 2465–2467 (2011).
26. Desjardins, A. E. *et al.* Angle-resolved optical coherence tomography with sequential angular selectivity for speckle reduction. *Opt. Express* **15,** 6200–6209 (2007).
27. Goodman, J. W. *Statistical Optics* (Wiley, 2000).
28. Sheng, P. *Introduction to Wave Scattering, Localization, and Mesoscopic Phenomena* 2nd edn (Springer, 2006).

Acknowledgements

This research was supported by the IT R&D Program (R2013080003), the Global Frontier Program (2014M3A6B3063710), IBS-R023-D1-2015-a00, the Basic Science Research Program (2013R1A1A2062560) and the Nano-Material Technology Development Program (2011-0020205) through the National Research Foundation of Korea (NRF) funded by the Ministry of Science, ICT & Future Planning. It was also supported by the Korea Health Technology R&D Project (HI14C0748) funded by the Ministry of Health & Welfare, Republic of Korea. The authors thank C. Fang-Yen for discussions.

Author contributions

W.C., S.K. and S.J. conceived the experiment. S.K. and S.J. carried out the measurements and analysed the data with W.C. W.C.* and Q.P. performed the theoretical study and supported interpretation of the data. Y.L. assisted in the design of the optical set-up. H.K. prepared scattering layers. T.Y. prepared biological tissues. J.J. and J.L. provided gold-coated silica beads. S.K., S.J. and W.C. prepared the manuscript. All authors contributed to finalizing the manuscript. W.C. and W.C.* refer to Wonshik Choi and Wonjun Choi, respectively.

Additional information

Supplementary information is available in the online version of the paper. Reprints and permissions information is available online at www.nature.com/reprints. Correspondence and requests for materials should be addressed to W.C.

Competing financial interests

The authors declare no competing financial interests.